

1 **Isotope geochemistry of Mississippi Valley Type stratabound F-Ba-(Pb-Zn)**
2 **ores of Hammam Zriba (Province of Zaghuan, NE Tunisia)**
3

4 Nejib Jemmali^a ✉, Emmanuel John M. Carranza^{b,c,d}, Balkiss Zimmel^a

5 ^a *Université de Gafsa, Faculté des Sciences, Département de Géologie, Sidi Ahmed Zarroug-2112 Gafsa, Tunisia*

6 ^b *Economic Geology Research Centre, Department of Earth and Oceans, James Cook University, Townsville,*
7 *Queensland, Australia*

8 ^c *Geological Sciences, School of Agricultural, Earth and Environmental Sciences, University of KwaZulu-Natal,*
9 *South Africa*

10 ^d *Institute of Geosciences, State University of Campinas, Campinas, São Paulo, Brazil*

11
12 **ABSTRACT**

13 The Hammam Zriba F-Ba-(Zn-Pb) ore deposit in the Province of Zaghuan in north-eastern
14 Tunisia is hosted in the shallow dipping unconformity between green marls with chalky biomicritic
15 limestones of Campanian age and Uppermost Jurassic carbonates. The mineralization consists mainly
16 of fluorite and barite with minor sphalerite and galena. Calcite is the main gangue mineral. Two types
17 of Zn-Pb sulfides can be distinguished according to the geometry of the orebodies, i.e., lenticular or
18 stratiform ores, intra-karstic fillings. Sulfur isotope compositions ($\delta^{34}\text{S}$) of barite range from 14.7 to
19 17.2‰, indicating that sulfur was derived from Triassic evaporites and the higher ones (19 to 25.7‰)
20 are due to reservoir effect associated with thermo-chemical sulfate reduction (TSR) or bacterial sulfate
21 reduction (BSR) under conditions of restricted sulfate supply. $\delta^{34}\text{S}$ of galena and sphalerite in
22 lenticular and intra-karstic orebodies range from -13.8 to 2.1‰, and could be explained by multiple
23 sources of reduced sulfur: Triassic evaporites, diagenetic primary sulfides as well as sulfur from
24 organic matter. Both TSR and BSR as potential contributors of sulfur are needed for sulfide
25 precipitation. Lead isotope compositions of galena exhibit very similar: $^{206}\text{Pb}/^{204}\text{Pb}$ (18.858–18.876),
26 $^{207}\text{Pb}/^{204}\text{Pb}$ (15.667–15.684), and $^{208}\text{Pb}/^{204}\text{Pb}$ (38.680–38.747) ratios, and plot between the upper crust
27 and orogene average growth curves, reflecting involvement of a mixing and subsequent

✉ Corresponding author. Faculté des Sciences de Gafsa, Sidi Ahmed Zarrouk, 2112 Gafsa, Tunisie. E-mail address: nejib.jemmali@yahoo.fr (Nejib Jemmali).

28 homogenization of Pb isotopic compositions of different source Pb reservoirs. The underlying 29
Paleozoic basement rocks were the plausible source of metals. The economic ore (fluorite F1) 30
mineralization was formed during the Eocene-Miocene compressional phase. During this deformation 31
phase, deep-seated basinal brines have been circulated as hydrothermal fluids that have interacted with 32 the
Paleozoic rocks, thereby leaching metals, and have been channelized through subsidiary faults 33 associated
with the major regional NE–SW-trending deep-seated Zaghouan-Ressas fault. 34 Hydrothermal fluids then
migrated to the site of deposition where they got mixed with shallow, cooler, 35 metal-depleted, TSR- and
BSR-derived sulfur-rich fluids, which triggered the precipitation of the ores.

36

37 **Keywords**

38 Hammam Zriba, Province of Zaghouan, Fluorite-Barite, Stratabound mineralization, Isotope
39 geochemistry

40

41 **1. Introduction**

42 The tectonic evolution of the Zaghouan-Ressas structural belt (ZRSB), which is situated in north-
43 eastern Tunisia (Fig. 1), is mainly a consequence of the following major tectonic events (Morgan et al., 1998; Frizon de Lamotte et al., 2009). The Triassic-Early Jurassic period was characterized by the 45
development of N–S trending normal faults and E–W trending transfer faults, which defined the 46 eastern
margin of a Jurassic carbonate platform. During the middle Jurassic – Early Cretaceous 47 extensional
period, the inherited E–W trending fault, which was controlled by major faults linked to 48 the basement,
continued to be active. This defined paleo-heights characterized by condensed 49 sequences and elongated
basins (Bouaziz et al., 2002) and the absence of the major part of Cretaceous 50 rocks at Hammam Zriba,
which are consistent with the persistence of the ZRSB at paleo-heights at 51 that time (Morgan et al.,
1998). The geodynamic context during the Late Cretaceous – Early Eocene 52 was characterized by
convergence, as expressed by NE–SW trending folds. The Late Eocene – Early 53 Miocene compressive
event was marked by an angular unconformity at the base of the Oligocene and 54 the development of an
Oligo–Miocene foreland basin. Contractional deformation of foreland basin

55 sediments in the ZRSB occurred in Early Miocene (post-Tortonian, pre-Messinian), and that 56 represented the main deformation responsible for the formation of the Atlas fold-thrust belt in Tunisia 57 (Morgan et al., 1998).

58 Several economically significant sediment-hosted F-Ba-Sr-(Zn-Pb-Cu-Hg) deposits occur along 59 the ZRSB (Fig. 1). Their mineralization is typically fluorite-rich and sulfide-poor, and shares 60 characteristics with MVT deposits such as the carbonate nature of the host rocks, the basinal brine 61 nature of fluids, the temperature of mineralizing fluids, the epigenetic character of mineralization, the 62 crustal source of metals and no magmatism associated (Souissi et al., 1997, 2010, 2013; Jemmali et al., 63 2011a). The province of Zaghouan is one of the most important fluorite-producing regions in Tunisia. 64 The deposits include the large Hammam Zriba F-Ba (Zn-Pb) deposit, Sidi Taya F-Pb (Zn-Ba-Sr) 65 deposit, Jebel Mecella F-Zn-Pb deposit, Hammam Jedidi F-Ba (Zn-Pb) deposit, Jebel Stah F deposit, 66 Jebel Oust F-Cu-Hg deposit, and the Jebel Ressay Pb-Zn (Fe) deposit (Fig. 1). Most of these deposits 67 are hosted in the Lower Liassic or Upper Jurassic massive limestones and the overlying Upper 68 Sinemurian-Carixian condensed limestones and Campanian marls. Because they have no direct 69 relationship with magmatism they are considered to have formed from basinal brines that were 70 mobilized during the Alpine orogeny (Souissi et al., 1997; Jemmali et al., 2011a).

71 Fluid inclusion measurements in fluorite from Hammam Zriba indicate that the ore-forming fluids 72 were hot ($>100^{\circ}\pm 20^{\circ}\text{C}$) and saline (>13 wt % NaCl equiv) basin-derived brines (Bouhleb et al., 1988). 73 These brines acquired high salinities and high molar ratios (Ca/Na, SO_4/Cl , Cl/Na), except for lower 74 Mg/Na ratio, at depth from the leaching of the Triassic evaporites by ascending hot fluids (Souissi et 75 al., 1997). The measured homogenization temperatures (110–185°C; Bouhleb et al., 1988) combined 76 with the thickness of the overburden, which never exceeded 2,100 m at the time of ore deposition, 77 imply a highly anomalous geothermal gradient that range between 50 and 70 °C/km. Consequently, 78 the reservoir of the fluids should be 3500–5000 m deep below the ore bearing layers (Souissi et al., 79 1997).

80 In the current study, fluorite-bearing Zn-Pb ores from Hammam Zriba have been investigated for
81 their sulfur and lead isotopes composition to elucidate the source of reduced sulfur, mechanisms of ore
82 deposition and possible age of mineralization.

83 **2. Hammam Zriba deposit geology**

84 The Hammam Zriba F-Ba-Zn-Pb deposit is located about 8 km SE of Zaghouan town and 60 km
85 south of Tunis. It is situated in a horst structure, with varying thickness (0.3 to 1 km) and NNW–SSE
86 strike over ~3 km (Fig. 2). This horst has formed during late Jurassic as an emerged block bounded by
87 major faults that were remobilized later during various deformation stages (Melki and Zargouni, 1991) 88
and limited mainly by two normal faults (Gharbi et al., 1981): one (F1) striking N135–145°E and 89
dipping 50–70°NE and another (F2) striking N130–150°E and dipping 50–70°SW. A N160–N180 90
trending fault in the Portlandian lithofacies has controlled the paleo-morphological framework of the 91
uppermost part of the Portlandian massive facies. The overlying Campanian unit exhibits onlap 92
structures that rest on the irregular eroded karstified and mineralized surface, which forms a screen 93
surface for the upward channelization of fluids and subsequent mineral deposit formation in karst and 94
graben (Melki and Zargouni, 1991). Rocks in the Hammam Zriba mine are intensely fractured at 95
different scales on the surface and in the subsurface (Fig. 2). The stratigraphy comprises a series of 96
sedimentary rocks from the Portlandian to the Eocene with a hiatus from the Berriasian to the middle- 97
Campanian, corresponding to an emersion period (Thibieroz, 1974, 1976) (Figs. 2 and 3). The 98
Portlandian series consists of massive, thick, biomicritic and grey limestones. The Campanian 99
comprises green marls with chalky biomicritic limestones. The bottom of the Campanian series
100 contains some thin and discontinuous black phosphatic-shale levels. The Maastrichtian and Paleocene
101 series are composed of beige limestones and interbedded grey and green marls respectively. The
102 Eocene is dominated by grey, thick, phosphate-bearing limestones beds and green marls.

103 The Hammam Zriba has been classified by Souissi et al. (1997) as a typical MVT deposit.

104 Underground mining of this deposit was operated from 1967 to 1992, when more than 4 Mt of
ore 105 grading 25% fluorite (CaF₂), 1–2% Pb+Zn has been produced (Maghreb Minerals, 2008).

106 3. Sampling and analytical methods

107 A total of 38 representative samples from sulfide (galena: n=10; sphalerite: n=5) and sulfate
108 (barite: n=23) minerals were collected from mine workings and outcrops of lenticular and intra-karstic
109 ores. Mineral separates of galena, sphalerite and barite were prepared for conventional sulfur isotope
110 analysis by careful hand-picking under a binocular microscope, and were analyzed at the laboratory of
111 the Institute of Mineralogy and Geochemistry of the University of Lausanne (Switzerland) using a
112 Carlo Erba 1100 elemental analyzer (EA) connected to a Thermo Fisher Delta S isotope ratio mass
113 spectrometer (IRMS) that was operated in the continuous He flow mode via a ConFlo III split interface
114 (EA-IRMS). The sulfur isotope compositions are reported as per mil (‰) deviations relative to the
115 Canyon Diablo troilite (V-CDT) standard. The overall analytical reproducibility of the EA-IRMS
116 analyses, assessed by replicate analyses of two laboratory standards (barium sulfate, with a working
117 $\delta^{34}\text{S}$ value of +12.5‰; pyrite E, -7.0‰) is better than $\pm 0.2\%$ (1 SD). The accuracy of the $\delta^{34}\text{S}$
118 analyses was checked periodically by analyses of the international reference materials IAEA-S-2 silver sulfides
119 (+22.7 $\pm 0.2\%$, values from IAEA-Catalogue and Documents) and NBS-123 sphalerite
120 (+17.09 $\pm 0.31\%$, value from NIST-Catalogue and Documents).

121 For Pb isotope measurements, 2–3 mg of galena sample was dissolved using ultrapure (double
122 distilled) HCl. The Pb isotope compositions were analyzed using a multi-collector inductively coupled
123 plasma mass spectrometer instrument within the Radiogenic Isotope facility at the University of Bern
124 (Switzerland). Sample aliquots were subsequently mixed with ~1.5 ml of a 2% HNO_3 solution spiked
125 with the NIST SRM 997 Thallium standard (2.5 ppb), and aspirated (~100 $\mu\text{l}/\text{min}$) into the ICP source
126 using an Apex™ desolvating nebulizer (Nu Instruments Ltd). Simultaneous measurements of all the
127 Pb and Tl isotopes, and ^{202}Hg ion signal were achieved by using seven Faraday collectors. The $^{205}\text{Tl}/$

128 ^{203}Tl ratio was measured to correct for instrumental mass bias (exponential law; $^{205}\text{Tl}/^{203}\text{Tl}=2.4262$).

129 Upon sample introduction, data acquisition consisted of 2 half-mass unit baseline measurements prior

130 to each integration block, and 3 blocks of 20 scans (10 s integration each) for isotope ratio analysis.

131 ^{204}Hg interference (on ^{204}Pb) was monitored and corrected using ^{202}Hg . At the beginning of the

132 analytical session, a 25 ppb solution of the NIST SRM 981 Pb standard, which was also spiked with

133 the NIST SRM 997 Tl standard (1.25 ppb), was analyzed. The external reproducibility of individual
134 analytical sessions was ca. 1×10^{-4} .

135 4. Results

136 4.1. Ore petrography

137 The mineralization is structurally- and lithologically-controlled and hosted in the shallow dipping
138 unconformity between Campanian green marls with chalky biomicritic limestones and Jurassic reef 139
limestones (Fig. 2). It consists of fluorite and barite as the dominant ore minerals associated with 140
accessory celestite and some minor sulfides, including both sphalerite and galena. Dill et al. (2014) 141
also reported the presence of minor minerals such as mimetite (zincian), pyromorphite, smithsonite, 142
and traces of hemimorphite. Calcite and quartz are the gangue minerals.

143 The synthesis of our detailed examination of hand specimens of ore samples (Fig. 4) with the
144 studies of Thibieroz (1975) and Bouhleb et al. (1988) reveals the following fluorite types:

145 - fluorite 1, the main economic ore, is a banded ore made of coarse-grained fluorite
146 alternating with bands of spherulitic barite 1 and quartz, associated with galena 1 and sphalerite 1 in
147 the black siliceous facies (diagenetic type mineralization (Mo) according to Bouhleb et al. (1985)) and
148 bands of white fibrous barite 2, which contains galena 2 crystals;

149 - fluorite 2, which is made of large crystals within karstic pockets cutting over the fluorite
150 1 and associated with galena 2 and sphalerite 2 and massive barite 3; and

151 - fluorite 3 consisting of large cubic crystals within geodes in the banded ore and the
152 karstic pockets.

153 Three types of ores can be distinguished according to the geometry of the orebodies:

154 (i) lenticular or stratabound ores are the most important and widespread, in close association with

155 sub-horizontal hydraulic fractures. This type of mineralization occurs between the Portlandian (wall)

156 and the Campanian (roof) (Fig. 4A), and exhibits banded texture composed of black siliceous facies

157 (Fig. 4B) and white fibrous barite 2 (Ba2) alternating with fluorite 1 (F1). Epigenetic galena 2, with

158 cubic crystals (Gn2), was found disseminated in barite 2 (Ba2) (Fig. 4C).

159 (ii) intra-karstic ores in the Portlandian limestones correspond to fillings of cavities, which are not
160 parallel to the bedding, and consist of fluorite 2 (F2) (Fig. 4E, F, H) associated with rare, fine galena 3
161 (Gn3) and sphalerite crystals (Sp2) (Fig. 4D, E, F, H); massive white barite 3 (Ba3) (Fig. 4E, G, H, I)
162 and large rhombohedra of calcite 1 (Ca1) crystals (Fig. 4J) ;

163 (iii) vein fillings in fractures cutting the Portlandian limestones, with calcite 2 (Ca2) (Fig. 4K, L)
164 and limestone onyx (LO) (Fig. 4K, L).

165 Based on the textural, mineralogical associations observed within the deposit and based on the
166 previous works of Bouhleb et al. (1988), mineralization has been classified into three stages (Table 1):

167 (1) pre-ore stage (diagenetic period) consisting of quartz, galena 1, sphalerite 1, barite 1 and pyrite
168 associated with organic matter (Type Mo); (2) hydrothermal ore stage composed of four sub-stages:
169 sub-stage 2a disseminated galenas 2 and 3 and sphalerite 2, sub-stage 2b barites 2 and 3, sub-stage 2c
170 fluorites 1, 2 and 3, and sub-stage 2d calcites 1 and 2; and (3) post-ore stage composed of secondary
171 minerals (smithsonite, hemimorphite and pyromorphite).

172 4.2. Sulfur isotope compositions

173 The $\delta^{34}\text{S}$ data obtained in this study (Table 2) represent various lenticular and intra-karstic ores,
174 and sulfur-mineral assemblages of the Hammam Zriba ore deposit. The $\delta^{34}\text{S}$ data range from -13.8 to
175 -1.4‰ for galenas 1 and 2, 1.7 to 2.1‰ for sphalerite, and 14.8 to 25.7‰ for all barites (Fig. 5).

176 For the lenticular ore, the $\delta^{34}\text{S}$ values of galena 2 range from -13.8 to -11.2‰ (average = $-$

177 12.73‰). The barite 1 has $\delta^{34}\text{S}$ values ranging from 15.4 to 16.9‰ (average = 16.4‰), which are
178 close to the average $\delta^{34}\text{S}$ value of Triassic evaporates of Jebel Ressay (16.4‰; Jemmali et al., 2011a).
179 The barite 2 is more enriched in ^{34}S , with $\delta^{34}\text{S}$ values between from 19 to 25.7‰ with average of
180 22.35‰.

181 For the intra-karstic ore, the $\delta^{34}\text{S}$ values range from -2.6 to 2.1‰. Disseminated galena 3 and
182 sphalerite 2 associated with the black shales show narrow ranges of $\delta^{34}\text{S}$ values (-2.6 to -1.4‰ with
183 an average -2.17 and 1.7 to 2.1‰ with an average 1.92‰, respectively). The associated barite 3 has

184 $\delta^{34}\text{S}$ values ranging from 14.6 to 17.2‰ (average = 15.6‰). This mean $\delta^{34}\text{S}$ of barite 3 is close to the
185 average $\delta^{34}\text{S}$ a value of Triassic evaporates of Jebel Ressay (Jemmali et al., 2011a).

186 4.3. Lead isotope compositions

187 The results of lead isotope analyses of the Hammam Zriba galena samples are given in Table 3 and
188 plotted on Figure 6. For comparison, the lead isotopic values of galena from other Tunisian carbonate-
189 hosted deposits studied by Jemmali et al. (2011a) and Souissi et al. (2013) and from Nefza magmatic
190 rocks studied by Decrée et al. (2014) are also shown. Lead from the Hammam Zriba deposit is
191 isotopically homogeneous and show fairly uniform $^{206}\text{Pb}/^{204}\text{Pb}$ (18.858–18.876), $^{207}\text{Pb}/^{204}\text{Pb}$ (15.667–
192 15.684), and $^{208}\text{Pb}/^{204}\text{Pb}$ (38.680–38.747) ratios (Table 2; Fig. 6), which clearly indicate a crustal
193 source of lead.

194 5. Discussion

195 5.1. *urces of sulfate*

196 The $\delta^{34}\text{S}$ values of barite in Hammam Zriba are considerably variable. The $\delta^{34}\text{S}$ values of barites 1
197 and 2 from lenticular ores and barite 3 from intra-karstic ore are mostly in the range between 14.6 to
198 25.7‰ (Table 2). Two populations may be identified (Fig. 5). One population (barites 1 and 3)
199 corresponds to $\delta^{34}\text{S}$ values in the range between 14.6 and 17.2‰ with an average of 16‰; the second
200 population (barite 2) includes only six barite samples with substantially higher $\delta^{34}\text{S}$ values in the range

201 between 19 and 25.7‰ with an average of 22.35‰. The $\delta^{34}\text{S}$ average values of barites from the
202 population 1 overlaps with the typical composition of Triassic evaporitic rocks of Jebel Ressay
203 (Jemmali et al., 2011a), which show a well-defined and narrow range of $\delta^{34}\text{S}$ values from 15 to 17.9‰
204 (Fig. 5). This suggests that the majority of dissolved sulfate in the hydrothermal fluids that formed the
205 base metal mineralization in Hammam Zriba was derived from groundwater that had interacted with
206 Triassic evaporites. The second population includes barite samples with S isotope ratios higher than
207 the first population values and different from those of Triassic evaporates.

208 The repeated cycles of Triassic gypsum dissolution/re-precipitation by meteoric waters may have
209 generated residual brines that were slightly depleted in ^{34}S (Thode and Monster, 1965), with high Sr-
210 Ba/Ca, as necessary for Sr-Barite mineralization (Hanor, 2000). During the crystallization of sulfates
211 the residual fluid was not enriched, but was slightly depleted in ^{34}S ; thus, the isotopic shift in the
212 second population of barite indicates that it did not precipitate from residual brines. Considering the
213 epigenetic character of the Hammam Zriba deposit, the formation of Ba-Sr and Pb-Zn-rich brines was
214 likely coupled to a mechanism that simultaneously led to a significant fractionation of the S isotopes
215 (Dill et al., 2009). The high $\delta^{34}\text{S}$ values can be due to reservoir effect associated with thermo-chemical
216 sulfate reduction (TSR) or bacterial sulfate reduction (BSR) under conditions of restricted sulfate
217 supply (Dill et al., 2009).

218

219 *5.2. Source (s) of sulfur*

220 The most important characteristic of the lenticular ores at Hammam Zriba is that they have
221 substantially more negative $\delta^{34}\text{S}$ values for galena in the range between -13.8 and -11.2‰ compared
222 to the intra-karstic ores, which have $\delta^{34}\text{S}$ values for galena that range between -2.6 and -1.4‰ , and
223 positive $\delta^{34}\text{S}$ values for sphalerite in the range between 1.7 and 2.1‰ (Table 2; Fig. 5). The differences
224 of $\delta^{34}\text{S}$ values of galenas in lenticular and intra-karstic ores could be explained by two processes: (1)
225 multiple sources of sulfur and (2) a single source of sulfur that evolved over time.

226 The most likely sources of reduced sulfur for the sulfide phases is Triassic evaporites, which were
227 suggested as the likely source of sulfur in the Zaghouan district (Jemmali et al., 2011a; Souissi et al.,
228 2013) and other carbonate-hosted Pb-Zn deposits in the Nappe and Dome zones (Jemmali et al.,
229 2011b, Jemmali et al., 2013a, Jemmali et al., 2013b). The observed isotopic compositions for sulfide
230 minerals at Hammam Zriba may be explained by reduction of these sulfate sources through TSR
231 and/or BSR.

232 It is well established that BSR takes place at 60–80 °C, and may occur at temperatures as high as
233 110°C (Jørgensen et al., 1992). TSR takes place at higher temperatures (mainly 80–130°C), though it

234 becomes more active at even higher temperatures. The average temperature of fluorite precipitation of
235 100–185°C overlaps to some extent with both BSR and TSR regimes. The temperature deduced from
236 galena-sphalerite pair is ~128°C using the equation of Grootenboer and Schwarcz (1969), which rather
237 falls into the TSR regime. Moreover, TSR causes isotopic fractionation from ~0 to ~20 per mil
238 (Kiyosu and Krouse, 1990; Machel et al., 1995), whereas BSR mechanism induces isotopic
239 fractionation of ~40 per mil. The calculated isotopic fractionation range of 14.5–29‰ falls into the
240 range of both regimes. Considering the temperature range and the negative values recorded in galena
241 (up to –13.8‰), it is wise to consider both mechanisms (TSR and BSR) as potential contributors of
242 sulfur needed for sulfide precipitation.

243 Mixing of TSR- and BSR-derived sulfur may account for the bulk isotopic sulfur composition.
244 In fact, the sulfides in the Zaghouan province display negative values (up to –13.8 ‰) as well as very
245 positive values in other similar ore deposits (up to +11.4‰; cf. Souissi et al., 2013). In this context,
246 the very negative $\delta^{34}\text{S}$ values of galena 2 (average = –12.73‰) compared to that of galena 3 (average
247 = –2.17‰) recorded in Hammam Zriba may indicate an increase of light sulfur from (i) mainly BSR-
248 derived sulfur and to some extent (ii) organic sulfur, and/or diagenetic sulfides ($\delta^{34}\text{S} < -2.36\text{‰}$;
249 Bouhleb, 1993) in the dark siliceous facies associated with organic matter. The proportion of light
250 sulfur and thus the superficial, depleted metal, bacteriologically-rich derived sulfur fluid, became more
251 pronounced in the early stage (galena 2).

252 Following the multi-sulfur source hypothesis, not only TSR- and BSR-derived sulfur but also
253 organic sulfur is considered as local source of sulfur though probably minor. The occurrence of oil
254 fluid inclusions in all type of fluorites of Hammam Zriba (cf. Bouhlef et al., 1988) could indicate the
255 contribution of organically bonded sulfur. In regard to this organically bonded sulfur and given the
256 fact that the ore is associated with black shales, thermal cracking of organic matter (e.g., presence of
257 hydrocarbon in fluid inclusion) can be considered as a possible local source of sulfur. The organic
258 sulfur and diagenetic sulfides along with BSR could have lowered the sulfur isotopic composition of

259 the epigenetic sulfides. The hydrocarbons observed in fluorite inclusions may indicate transport from a
260 deeper mature source rock.

261 *5.3. Sources of metals and age of mineralization*

262 On conventional uranogenic and thorogenic plots (Fig. 6), data for most of the analyzed samples
263 fall between the upper crustal and orogen model curves of Zartman and Doe (1981). The tight linear
264 clustering of Pb isotope data for the galena ores may reflect involvement of mixing and subsequent
265 homogenization of Pb isotopic composition of different source Pb reservoirs that would also explain
266 the uniform isotopic values (Fig. 6).

267 The lead isotope composition data suggest that the lead in the Hammam Zriba deposit was derived
268 from a different source than the lead in other Tunisian carbonate-hosted deposits and in the Nefza
269 magmatic rocks, and has been interpreted to probably indicate regional differences in the composition
270 of the underlying sediments, which probably include the Paleozoic basement (Jemmali et al., 2011a;
271 Souissi et al., 2010; Souissi et al., 2013). The Pb isotope ratios of galena from Jebel Ressayas and Sidi
272 Taya deposits in the Zaghouan district are markedly higher and different than those from the Hammam
273 Zriba deposit (Fig. 6), and are enriched in radiogenic lead indicating that the former were derived from
274 a source enriched in both U and Th. The geographic position of the deposits was closely related to this
275 variation and the differences in lead isotopic composition may reflect the spatial dissimilarity of
276 involved crustal rocks (Jeong et al., 2012). This crustal source provenance is supported by strontium

277 isotope data from minerals associated with the ore deposits in the Zaghouan District (i.e., Sidi Taya,
278 Hammam Jedidi, Oued M'tak and Jebel Oust) (Souissi et al., 2013), which could have been sourced
279 from connate waters trapped in the Paleozoic sedimentary column. Based on the data presented above,
280 the Paleozoic seems to be the dominant source.

281 Geological field observations, textural crosscutting and paragenetic sequence, supported by fluid
282 inclusions show the existence of three chronologically distinct stages of mineralization. Mineralization
283 with fluorite types are epigenetic and formed after the lithification and dissolution of the Portlandian
284 limestone host rocks, and are structurally-controlled due to the presence of N070–090 and N160–N180

285 trending faults (Melki and Zargouni, 1991). Thus, their emplacement postdates the Upper Jurassic
286 (i.e., Portlandian). According to Melki and Zargouni (1991), the horst structure of Hammam Zriba has
287 formed during the Late Jurassic as an emerged block bounded by major fault that was re-activated
288 during various later tectonic events. The ultimate last phase in which the horst took the final form was
289 the Tortonian period, which caused the mineral deposition (Melki and Zargouni, 1991). Furthermore,
290 based on Sr isotope ages that range between 28 and 19 Ma, Dill et al. (2014) attributed the Tunisian
291 salt-related deposits to the Chattian-Burdigalian age. Moreover, in the area of Oued M'Tak, the
292 youngest rock series hosting F-(Zn-Pb) deposit is Miocene (Burdigalian) in age. All these arguments
293 strongly suggest an Upper/Late Miocene age for the mineralization of Hammam Zriba deposit. The
294 same age was suggested for other Tunisian Pb-Zn deposits (Decrée et al., 2008; Jemmali et al., 2011a,
295 b; Jemmali et al., 2013b; Souissi et al., 2013; Jemmali et al., 2014).

296 *5.4. Proposed genetic model*

297 Based on the geological, mineralogical and geochemical relationships discussed above, and
298 published literature dealing with Hammam Zriba as cited in the discussion above, a proposed genetic
299 model is postulated as follows.

300 At Hammam Zriba, anticlines are interpreted as fault-inversion folds that seem to have occurred
301 during the late Eocene – early Miocene (Frizon de Lamotte et al., 2000), formed in normal sequence
302 on the external side of the ZRSB. Flow of Triassic strata into the cores of these folds may have been

303 assisted by tectonic loading during fault inversion along the ZRSB. Subsequently, structures in the
304 ZRSB were dissected by NE–SW trending faults that propagated through the post-rift sequence during
305 post-Miocene re-activation of syn-rift extensional faults. These faults were linked to extension in NW–
306 SE trending graben that cut the ZRSB (Morgan et al., 1998). The Eocene–Miocene compressional
307 phase “Alpine orogeny” caused the development of the foreland basin (Morgan et al., 1998). The
308 generated topographic gradient induced the circulation of deep-seated basinal brines as hydrothermal
309 fluids, as indicated by fluid inclusion temperatures of fluorites which are predominantly in the 100–
310 185 °C range (Bouhlef et al., 1988), and the hydrothermal fluids acquired their salinity mainly from

311 Triassic evaporates. The deep-seated basinal brines probably interacted with the basement rocks,
312 thereby leaching metals, and were channelized through secondary faults associated with the ZRSB
313 major regional NE–SW-trending deep-seated fault. Alternatively, the deep-seated, hot fluids migrated
314 to the site of deposition where they got mixed with shallow, cooler, metal-depleted, TSR- and BSR-
315 derived sulfur-rich fluid, which triggered the precipitation of the ores (Fig. 7). This mixing model is
316 supported by wall-rock silicification, which indicates that hot fluids underwent conductive cooling as
317 they encountered carbonate host rocks (Fournier, 1985; Rddad and Bouhlel, 2015), as well as by the
318 temperature fluctuations recorded in fluorite. The lower part of the Campanian consists of marls and
319 black shales, which acted as an impermeable barrier of the fluid circulation.

320 The proposed ore genesis model, which involves the interaction between basement-derived ore
321 fluids and shallower H₂S-rich fluids, has similarities to numerous MVT ore deposits worldwide (e.g.,
322 Pine Point, Canada (Rhodes et al., 1984), Ozarks, USA (Leach, 1994; Souissi et al., 2007), Touissit-
323 Bou Beker district, Moroccan-Algerian confines (Bouabdellah et al., 2012), Jebel Ressas, Tunisia
324 (Jemmali et al., 2011a), and Bou Dahar, Morocco (Rddad and Bouhlel, 2015)).

325 **6. Conclusions**

326 The study of sulfur and lead isotope geochemistry of sulfide minerals allowed to constrain the
327 genesis of sulfur and metals and the timing of fluorite-bearing Zn-Pb mineralization at Hammam
328 Zriba, which occurs as lenticular (or stratiform) and intra-karstic ores in the shallow dipping

329 unconformity between Campanian and Upper Jurassic carbonates. The following conclusions are
330 reached:

331 (i) Ore mineral assemblage consists of fluorite and barite associated with minor sulfides, including
332 sphalerite and galena. Calcite and quartz are the gangue minerals.

333 (ii) The $\delta^{34}\text{S}$ values of barite are much close to the $\delta^{34}\text{S}$ of Triassic evaporates. The $\delta^{34}\text{S}$ values of
334 galena and sphalerite minerals indicate that the deposition of sulfides has resulted from mixing of
335 TSR- and BSR-derived sulfur. The most likely sources of reduced sulfur for the sulfide phases are
336 Triassic evaporites, and locally diagenetic sulfides and organic sulfur.

337 (iii) The Pb isotope compositions of galena have homogenous $^{206}\text{Pb}/^{204}\text{Pb}$ (18.858–18.876),
338 $^{207}\text{Pb}/^{204}\text{Pb}$ (15.667–15.684), and $^{208}\text{Pb}/^{204}\text{Pb}$ (38.680–38.747) ratios, which suggest mixing and
339 subsequent homogenization of Pb isotopic composition of different source Pb reservoirs: deep-sourced
340 metal-rich brines from the underlying crustal rocks, possibly the Paleozoic basement.

341 (iv) The mineralization of Hammam Zriba deposit has likely an upper or late Miocene age.

342

343 **Acknowledgements**

344 We thank Professor Fouad Souissi (Faculty of Sciences of Tunis) for his assistance and
345 discussion about the metallogeny of Hammam Zriba. We are grateful to Larbi Rddad and the
346 anonymous reviewers for their comments, and to Associate Editor Jacek Puziewicz for expert handling
347 of our paper.

348

349 **References**

350 Boccaletti, M., Cello, G., Tortorici, L., 1990. First order kinematic elements in Tunisia and the Pelagian
351 block. *Tectonophysics*, 176(1), 215-228.

352 Bouabdellah, M., Sangster, D.F., Leach, D.L., Rown, A.C., Johnson, C.A., Emsbo, P., 2012. Genesis of the
353 Touissit-Bou Beker Mississippi Valley-Type District (Morocco–Algeria) and its relationship to the Africa
354 Europe collision. *Economic Geology* 107, 117–146.

355 Bouaziz, S., Barrier, E., Soussi, M., Turki, M. M., & Zouari, H., 2002. Tectonic evolution of the northern

- 356 African margin in Tunisia from paleostress data and sedimentary record. *Tectonophysics*, 357(1), 227-253.
- 357 Bouhlef, S., Fortuné, J.P., Guilhaumou, N., Touray, J.C., 1988. Les minéralisations stratiformes à F-Ba de
358 Hammam Zriba, Jebel Guébli (Tunisie nord orientale): l'apport des études d'inclusions fluides à la
359 modélisation génétique. *Mineralium Deposita*, 23(3), 166-173.
- 360 Bouhlef, S., 1993. Géologie, minéralogie et essai de modélisation des minéralisations à F-Ba-Sr-Pb-Zn-
361 (S) associées aux carbonates (Jurassiques et Crétacés) et aux diapirs triasiques: Gisements de Stah-Kohol,
362 Zriba-Guebli, Bou Jabeur et Fej lahdoum (Tunisie septentrionale). Thèse de doctorat. Faculté des Sciences
363 de Tunis. 303p.
- 364 Burrolet, P.F., 1991. Structures and tectonics of Tunisia. *Tectonophysics* 195, 359–369.

365 Claypool, GE., Holser, WT., Kaplan, IR., Sakai, H., Zak, I., 1980. The age curves of sulfur and oxygen isotopes
366 in marine sulfate and their mutual interpretation; *Chemical Geology* 28: 199-260.

367 Decrée, S., Marignac, C., De Putter, T., Deloule, E., Liégeois, JP., Demaiffe, D., 2008. Pb-Zn mineralization in a
368 Miocene regional extensional context: the case of the Sidi Driss and the Douahria ore deposits (Nefza
369 mining district, northern Tunisia). *Ore Geology Reviews* 34:285-303.

370 De Lamotte, D. F., Leturmy, P., Missenard, Y., Khomsi, S., Ruiz, G., Saddiqi, O., Guillocheau, F., Michard, A.
371 2009. Mesozoic and Cenozoic vertical movements in the Atlas system (Algeria, Morocco, Tunisia): an
372 overview. *Tectonophysics*, 475(1), 9-28.

373 Dill, H.G., Henjes-Kunst, F., Berner, Z., Stüben, D., 2009. Miocene diagenetic and epigenetic strontium
374 mineralization in calcareous series from Cyprus and the Arabian Gulf. Metallogenic perspective on sub- and
375 suprasalt redox-controlled base metal deposits. *J. Asian Earth Sci.* 34, 557–576.

376 Dill, H.G., Nolte, N., Hansen, BT., 2014. Lithology, mineralogy and geochemical characterizations of sediment-
377 hosted Sr–F deposits in the eastern Neo-Tethyan region–With special reference to evaporation and
378 halokinesis in Tunisia. *Journal of African Earth Sciences*, 92, 76-96.

379 Fournier, R.O., 1985. The behavior of silica in hydrothermal solutions. In *Geology and geochemistry of*
380 *epithermal systems*. Edited by B.R. Berger and P.M. Bethke. *Reviews in Econ. Geol.* 2, 45–61.

381 Frizon de Lamotte, D., Saint Bezar, B., Bracène, R., Mercier, E., 2000. The two main steps of the Atlas building
382 and geodynamics of the western Mediterranean. *Tectonics*, 19(4), 740-761.

383 Gharbi, M., Ben Ayed, N., Ben Said, EA., 1981. Essai d'interprétation tectonique du champ filonien de Bou-

- 384 Jaber (Atlas tunisien central). Actes du Premier Congrès national de la terre (Tunis). Tome 1, 393-403.
- 385 Grootenboer, J., Schwarcz, HP., 1969. Experimentally determined sulfur isotope fractionations between sulfide
386 minerals. *Earth Planet. Sci. Lett.* 7, 162–166.
- 387 Hanor, J.S., 2000. Barite-celestine geochemistry and environments of formation. In: Alpers, C., Jambor, J.,
388 Norstrom, K. (Eds), *Sulphate Minerals. Reviews in Mineralogy and Geochemistry*, vol. 40, pp. 193–275.
- 389 Jemmali, N., Souissi, F., Vennemann, T., Carranza, EJM., 2011a. Genesis of the Jurassic carbonate-hosted Pb-
390 Zn deposits of Jebel Ressay (North-Eastern Tunisia): evidence from mineralogy, petrography and trace metal
391 contents and isotope (O, C, S, Pb) geochemistry. *Resource Geology* 61, 367–383.
- 392 Jemmali, N., Souissi, F., Villa, IM., Vennemann, T., 2011b. Ore genesis of Pb-Zn deposits in the Nappe zone of
393 Northern Tunisia: constraints from Pb-S-C-O isotopic systems. *Ore Geology Reviews* 40, 41-53.

394 Jemmali, N., Souissi, F., Carranza, E.J.M., Vennemann, T.W., 2013a. Sulfur and lead isotopes of Guern Halfaya
395 and Bou Grine deposits (Dome zone, northern Tunisia): Implications for sources of metals and timing of
396 mineralization. *Ore Geology Reviews*, 54, 17-28.

397 Jemmali, N., Souissi, F., Carranza, E.J.M., Bouabdellah, M., 2013b. Lead and sulfur isotope constraints on the
398 genesis of the polymetallic mineralization at Oued Maden, Jebel Hallouf and Fedj Hassene carbonate-hosted
399 Pb–Zn (As–Cu–Hg–Sb) deposits, Northern Tunisia. *Journal of Geochemical Exploration*, 132, 6-14.

400 Jemmali, N., Souissi, F., Carranza, E.J.M., Vennemann, T.W., Bogdanov, K., 2014. Geochemical constraints on
401 the genesis of the Pb–Zn deposit of Jalta (northern Tunisia): Implications for timing of mineralization,
402 sources of metals and relationship to the Neogene volcanism. *Chemie der Erde-Geochemistry*, 74(4), 601-
403 613.

404 Jeong, Y. J., Cheong, C. S., Shin, D., Lee, K. S., Jo, H. J., Gautam, M. K., Lee, I., 2012. Regional variations in
405 the lead isotopic composition of galena from southern Korea with implications for the discrimination of lead
406 provenance. *Journal of Asian Earth Sciences*, 61, 116-127.

407 Jorgensen, B. B., Isaksen, M. F., Jannasch, H. W., 1992. Bacterial sulfate reduction above 100 degrees Celsius in
408 deep-sea hydrothermal vent sediments. *Science*, 258(5089), 1756-1758.

409 Kiyosu, Y., Krouse, H.R., 1990. The role of organic acid in the abiogenic reduction of sulfate and the sulfur
410 isotope effect. *Geochemical Journal*, 24(1), 21-27.

411 Leach, D.L., 1994. Genesis of the Ozark Mississippi Valley-Type metallogenic province. In: Fontebote, L.,
412 Boni, M. (Eds.), *Sediment Hosted Zn-Pb Ores*, Springer–Verlag, 104–138.

- 413 Machel, HG., Krouse, HR., Sassen, R., 1995. Products and distinguishing criteria of bacterial and
414 thermochemical sulfate reduction: *Applied Geochemistry*, v. 10, p. 373–389.
- 415 Maghreb Minerals plc., 2008. Zinc exploration in North Africa.
416 <http://equatorgold.co.uk/finex/downloads/presentations/2008/222.ppt>
- 417 Melki, F., Zargouni, F., 1991. Tectonique cassante post jurassique de la mine de Hammam Zriba (Tunisie nord-
418 orientale). Incidences sur la karstification et les concentrations de fluorine, barytine et célestine,
419 d'environnement carbonaté. *Bull. Soc. Géol. France*, 162(5), 851-858.
- 420 Morgan, M., Grocott, J., Moody, R., 1998. The structural evolution of the Zaghouan-Ressas Structural Belt,
421 northern Tunisia. *Geological Society London Special Publication*, Volume 132, pp. 405-422.

- 422 Ohmoto, H., Rye, RO., 1979. Isotopes of sulfur and carbon. In: Barnes, H.L. (Ed.), *Geochemistry of*
423 *Hydrothermal Ore Deposits*. Wiley, New York, pp. 509–567.
- 424 Ohmoto, H., 1986. Stable isotope geochemistry of ore deposits. *Reviews in Mineralogy and*
425 *Geochemistry*, 16(1), 491-559.
- 426 Perthuisot, V., 1978. *Dynamique et pétrogenèse des extrusions triasiques en Tunisie septentrionale*. Theses,
427 *Doctorat d'Etat, Ecole Normale supérieure de Paris, Travaux du Laboratoire de Géologie 12*, 312 pp.
- 428 Peter, J.M., Shanks, W.C., 1992. Sulfur, carbon and oxygen isotope variations in submarine hydrothermal
429 deposits of Guaymas Basin, Gulf of California, USA: *Geochimica et Cosmochimica Acta*, v. 56, no. 5, p.
430 2025–2040.
- 431 Rddad, L., Bouhlel, S., 2016. The Bou Dahar Jurassic carbonate-hosted Pb–Zn–Ba deposits (Oriental High
432 Atlas, Morocco): Fluid-inclusion and C–O–S–Pb isotope studies. *Ore Geology Reviews*, 72, 1072-1087.
- 433 Rhodes D., Lantos E.A., Lantos, J.A., Webb, R.J, Owens, D.C., 1984. Pine Point orebodies and their relationship
434 to the stratigraphy, structure, dolomitization and karstification of the Middle Devonian Barrier Complex.
435 *Econ. Geol.* 79, 991–1055.
- 436 Souissi, F., Dandurand, J., Fortuné, J., 1997. Thermal and chemical evolution of fluids during fluorite.
437 *Mineralium Deposita*, Volume 32, pp. 257-270.
- 438 Souissi F., Sassi R., Bouhlel S., Dandurand J-L., Ben Hamda S. (2007). – Fluid inclusion microthermometry and
439 rare earth element distribution in the celestite of the Jebel Doghra ore deposit (Dome zone, Northern
440 Tunisia) : towards a new genetic model. *Bull. Soc. Géol. Fr.*, t. 178, n° 6, pp. 459-471.

- 441 Souissi, F., Souissi, R., Dandurand, J., 2010. The Mississippi Valley-type fluorite ore at Jebel Stah (Zaghouan
442 district, north-eastern Tunisia): contribution of REE and Sr isotope geochemistries to the genetic model. *Ore
443 Geology Reviews*, Volume 37, pp. 15-30.
- 444 Souissi, F., Jemmali, N., Souissi, R., Dandurand, J., 2013. REE and isotope (Sr, S, Pb) geochemistry to constrain
445 the genesis and timing of the F-(Ba-Pb-Zn). *Ore Geology Reviews*.
- 446 Thibieroz, J., 1974. Hammam Jedidi et Hammam Zriba: Etude géologique et minière de deux gisements
447 stratiformes dans le cadre de la province fluorée tunisienne; l'association des concentrations fluorées aux
448 surfaces d'émersion. 1974. Thèse de 3e cycle univ. Paris VI. 367p
- 449 Thibieroz, J., 1976. Reconstitution chronologique du rôle des surfaces d'émersion dans l'histoire du gisement de
450 fluorine de hammam Zriba (région de Zaghouan Tunisie). *Mém. H. série soc. Géol. France*, 7, 33-37.

- 451 Thode, H.G., Monster, J., 1965. Sulphur isotope geochemistry of petroleum, evaporites and ancient seas. In:
- 452 Young, A., Galley, J.E. (Eds.), *Fluids in Subsurface Environments*, vol. 4. Am. Ass. Petrol. Geol., Tulsa,
- 453 Oklahoma, USA, pp. 367–377
- 454 Zartman, R.E., Doe, B.R., 1981. Plumbotectonics — the model. *Tectonophysics* 75, 135–162.
- 455

FIGURES CAPTIONS

456

457 Fig. 1. Tectonic and metallogenic map of Northern Tunisia (adapted from Burrolet, 1991; Perthuisot, 1978;
458 Jemmali et al., 2011; Decrée et al., 2016).

459 Fig. 2. Geologic map of the Hammam Zriba F-Ba-Sr (Zn-Pb) deposit, showing major faults and distribution of
460 ore bodies (adapted from Melki and Zargouni, 1991).

461 Fig. 3. Main lithostratigraphic column of the Hammam Zriba deposit (adapted from Melki and Zargouni, 1991).

462 Fig. 4. Appearance of representative field and hand specimens of all types of Hammam Zriba F-Ba- (Pb-Zn)
463 orebodies occurring within the unconformity between Portlandian and Upper Cretaceous rocks. A: stratabound
464 mineralization along the unconformity between Portlandian and Upper Cretaceous rocks. B: Banded ore with
465 fluorite 1 (F1), black siliceous facies "Type M0" with spherulitic barite 1 (Ba1), authigenic quartz and diagenetic
466 sulfides (galena and sphalerite) and barite 2 (Ba2) in lenticular orebody. C: white fibrous barite 2 (Ba2) with
467 cubic crystals of galena 2 (Gn2) in lenticular orebody. D: fluorite 2 (F2) with fine-grained galena 3 (Gn3) and
468 brown sphalerite (Sp2) in intra-karstic orebody. E: Cretaceous black shales (Sh) with fluorite 2 (F2), fibrous
469 barite 3 (Ba3) associated with fine grained galena 2 (Gn2) and brown sphalerite (sp2) in intra-karstic orebody. F:
470 fluorite 2 (F2) associated with brown sphalerite (Sp2) in intra-karstic orebody. G: intra-karstic ore with fibrous
471 barite 3 (Ba3), hosted by Portlandian limestones (L). H: coarse-grained galena 3 (Gn3) associated with barite 3
472 (Ba3) and fluorite 2 (F2) in intra-karstic ore. I: calcite rhombohedra (Ca1) associated to barite 3 (Ba3) in intra-
473 karstic ore. J: veins in Portlandian limestones filled with Calcite 2 (Ca2) and limestone Onyx (LO).

474 Fig. 5. Frequency distribution of $\delta^{34}\text{S}$ values for mineral separates of sphalerite 2, galenas 1 and 2, all types of
475 barites from the Hammam Zriba deposit. Also shown for comparison is the sulfur isotope range for Triassic
476 evaporates at Jebel Ressas (Jemmali et al., 2011a).

477 Fig. 6. Plots of lead isotope compositions of galena from the Hammam Zriba deposit, including analyses of Jebel
478 Ressas, Sidi Taya galenas from Jemmali et al. (2011b) and Souissi et al. (2013), and analyses of Nefza
479 magmatic rocks from Decrée et al. (2014). Evolution curves for upper crust and orogene from Zartman and Doe
480 (1981) are shown for reference.

481 Fig. 7. Schematic proposed genetic model of the Hammam Zriba F-Ba- (Pb-Zn) ore deposit (adapted and
482 modified based on present-day cross section of Jebel Zaghouan-Zriba from Morgan et al. 1998).

483

484

TABLE CAPTIONS

485 Table 1. Mineral paragenetic sequence in the Hammam Zriba deposit

486 Table 2. Sulfur isotope compositions of sulfides (galena and sphalerite) and sulfate (barite) from the Hammam

487 Zriba deposit, and gypsum from Jebel Ressay (Jemmali et al., 2011a).

488 Table 3. Ratios of Pb isotope compositions in galena from the Hammam Zriba deposit.

489

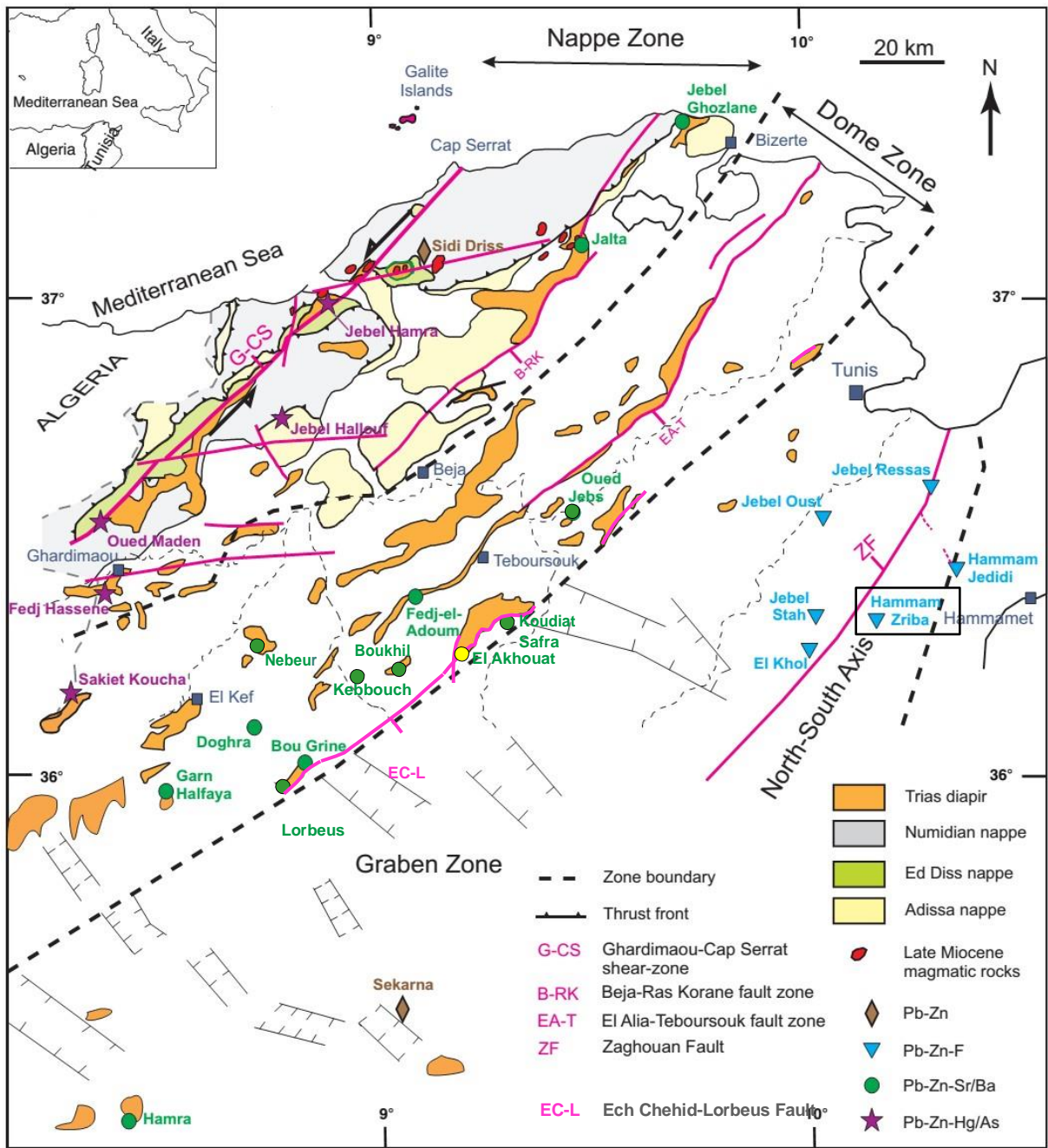


Figure 1

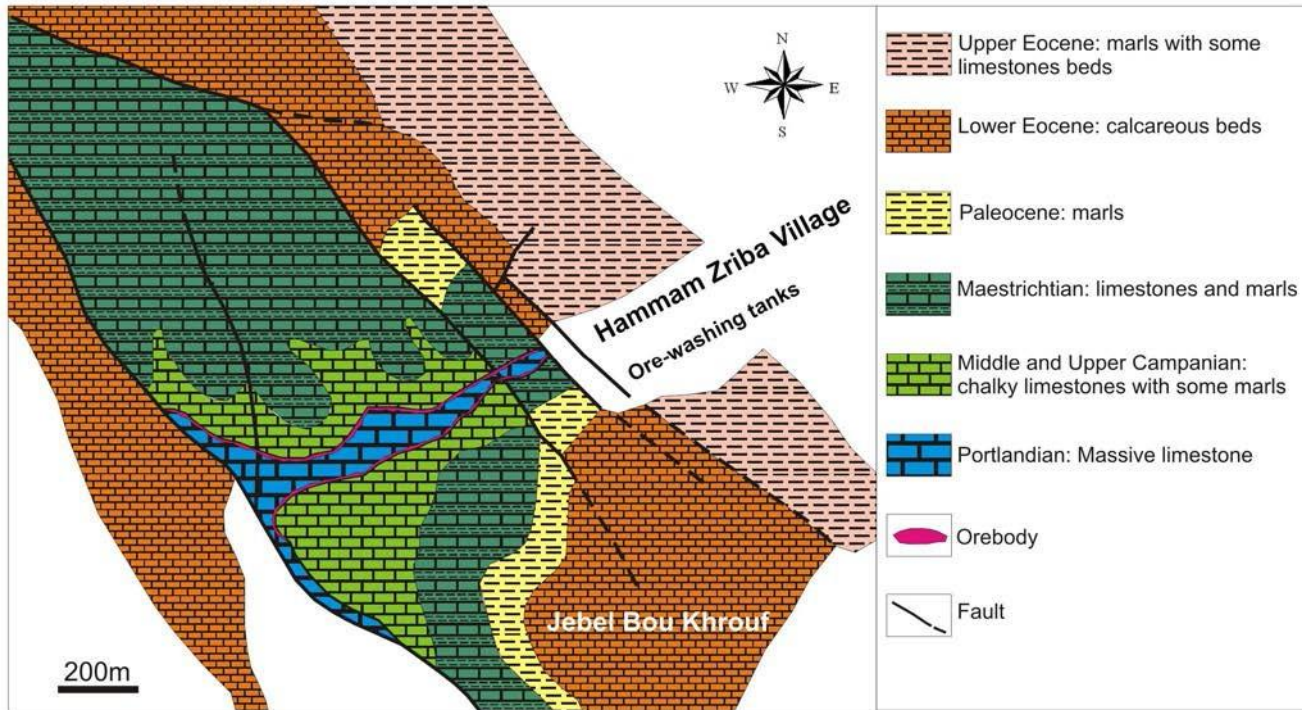
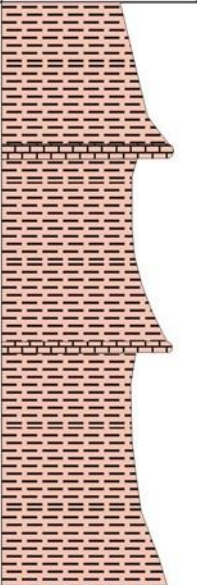
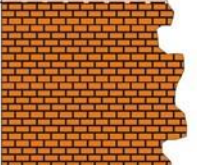





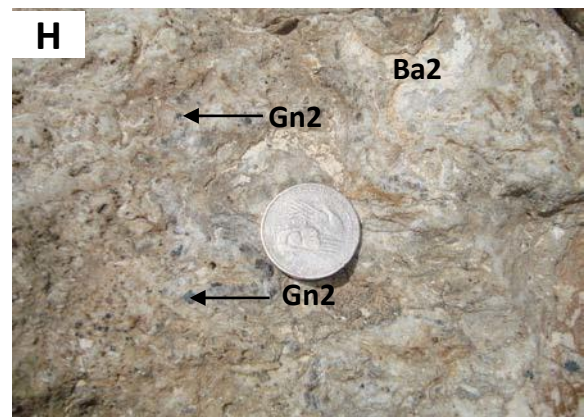
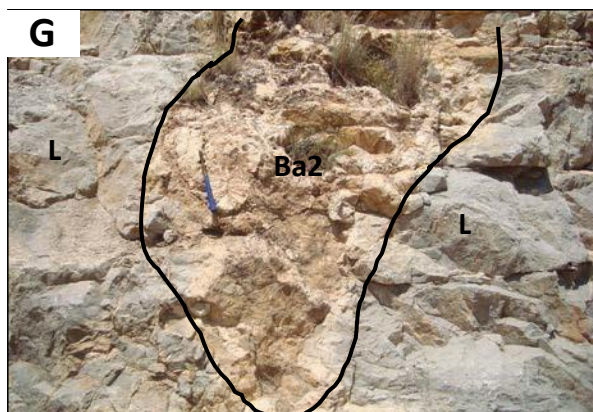
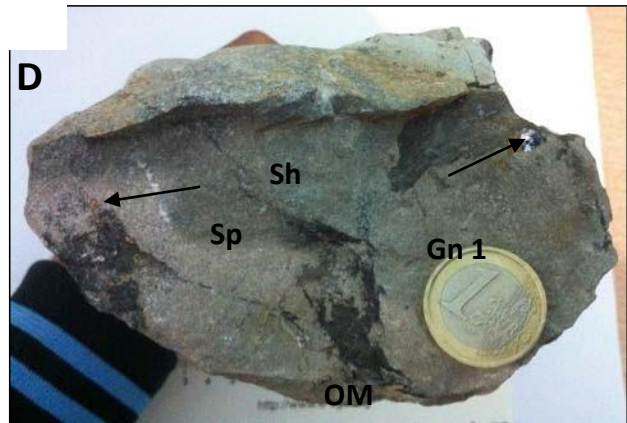
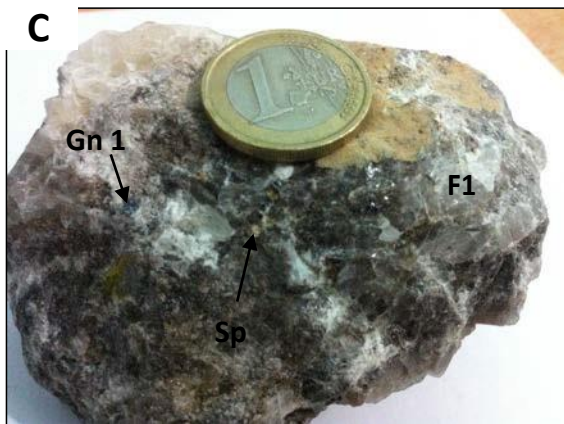
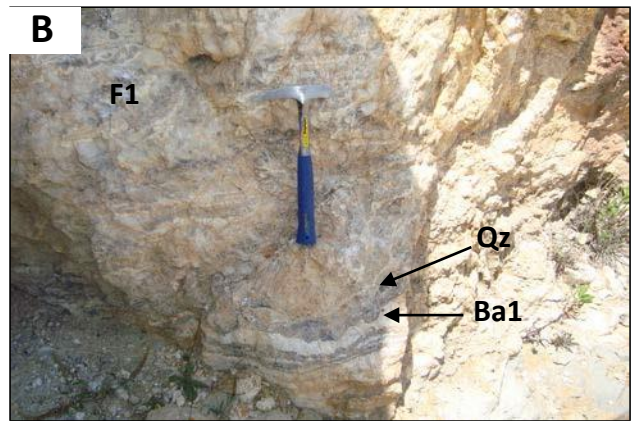


Figure 2

Age	Column	Main lithology
Upper Eocene		Yellow to green marls with some limestones beds
Lower Eocene		Grey, thick and massive phosphate-bearing calcareous beds
Paleocene		Green marls
Maastrichtian		Beige limestones with interbedded green marls
Campanian		Chalky limestone beds
Portlandian		Stratabound mineralization
		Bioclastic and massive grey limestones beds

100m

Figure 3



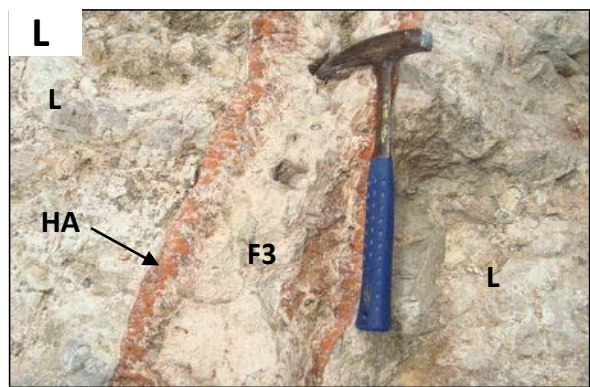
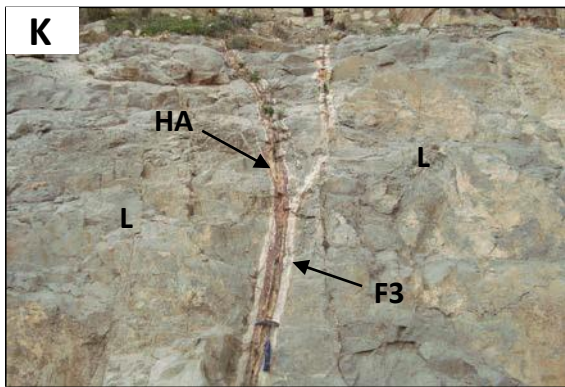
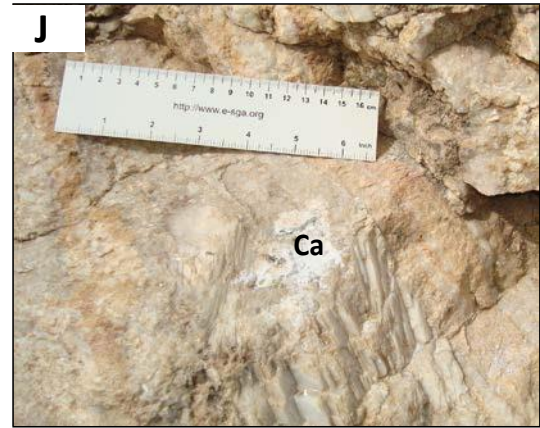


Figure 4

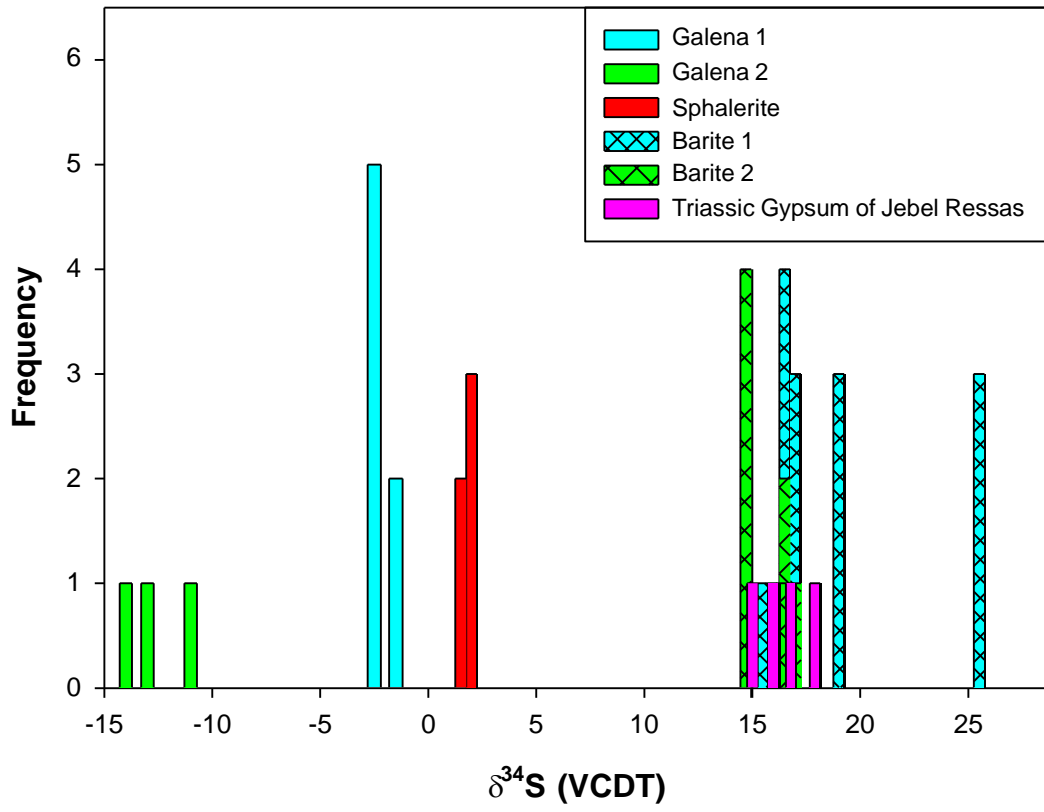


Figure 5

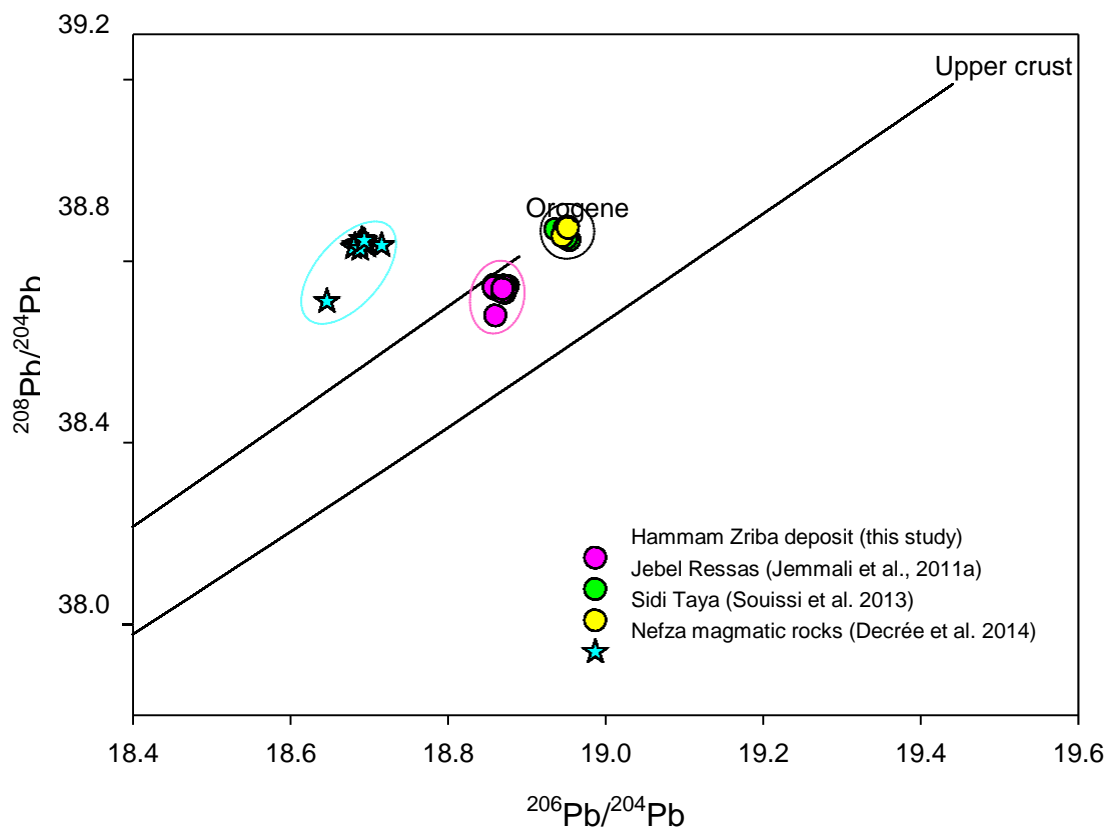
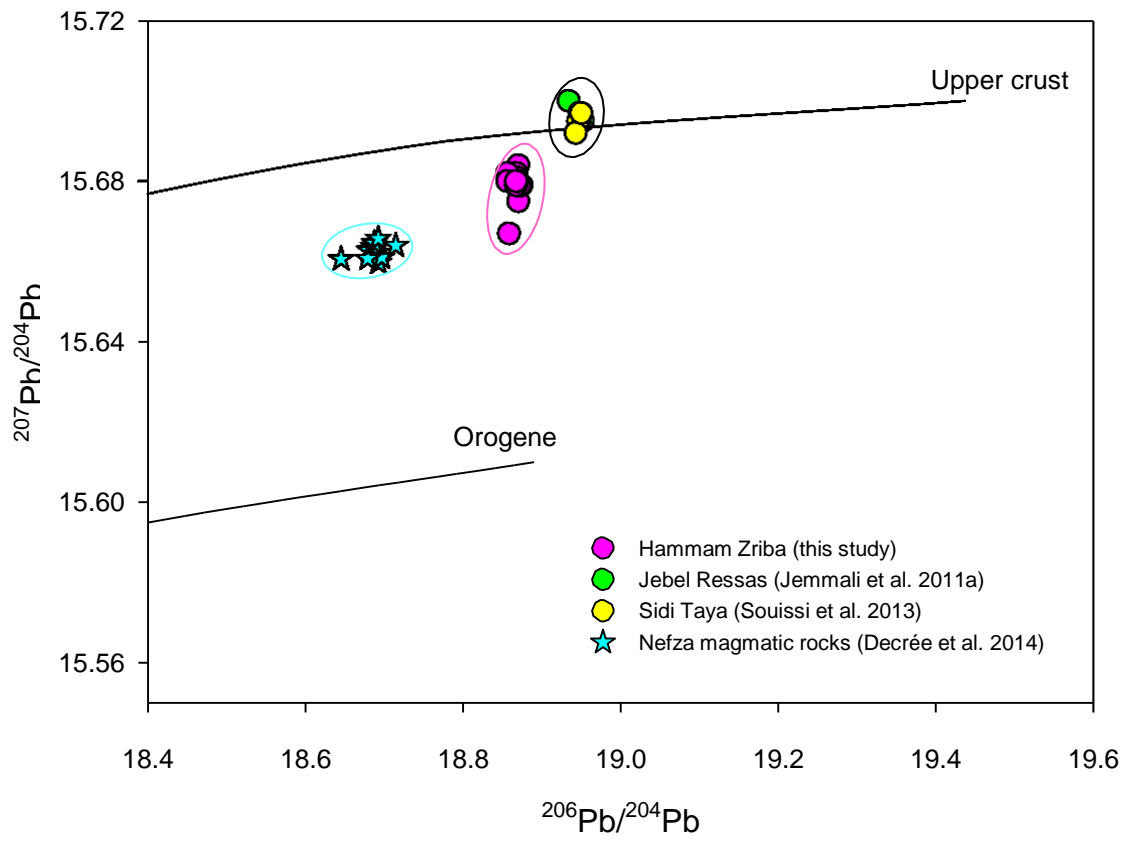


Figure 6

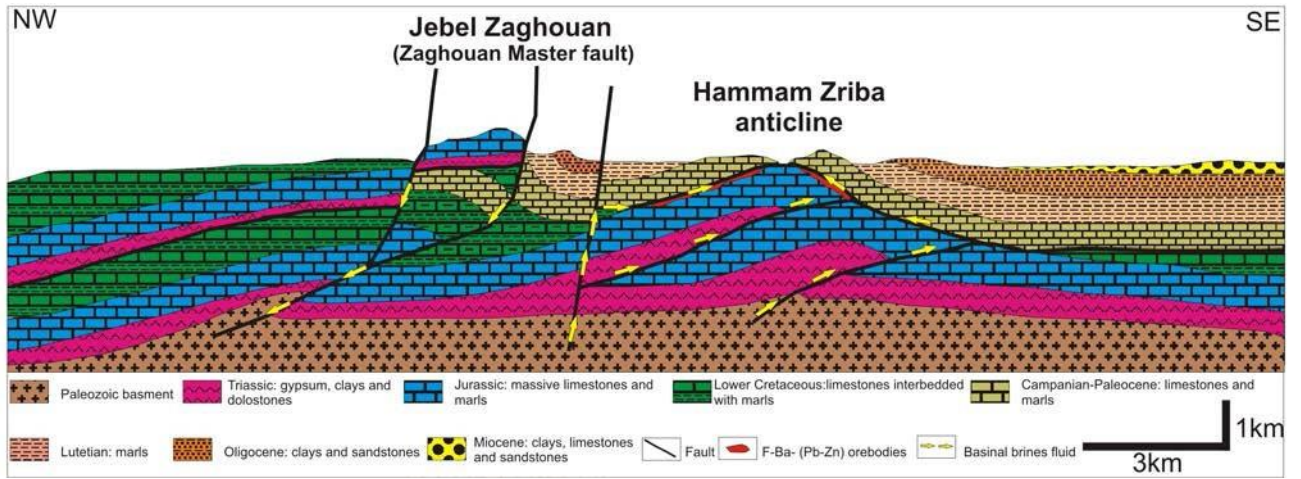


Figure 7